AIAA Journal
Vol. 62, No. 11, November 2024

Wavelet-Based Characterization of Spatiospectrotemporal Structures in F404 Engine Jet Noise

Tyce W. Olaveson* and Kent L. Gee†
Brigham Young University, Provo, Utah 84602

https://doi.org/10.2514/1.J063944

Spatiospectral lobes are significant contributors to noise radiated from full-scale tactical aircraft. Prior studies have explored lobe frequency-domain characteristics, but a joint time–frequency domain analysis has the potential to further describe these phenomena and connect them to source-related events in the time waveform. This paper uses acoustical data collected from a 120-microphone array near a T-7A-installed F404 engine to characterize the spatiospectral lobes in combinations of the time, frequency, and spatial domains. An event-based beamforming method is used in conjunction with a wavelet transform to determine propagation angles and event source locations corresponding to each of the lobes. Temporospectral events in the wavelet transform are then analyzed using Markov chains. Finally, spatiospectral maps created from the measured data are decomposed into individual lobes using events in the wavelet transform as a guide. The spatiospectrotemporal combination of these three analyses shows that the lobes originate from multiple, overlapping regions along the jet lipline and that each lobe has its own peak radiation angle. Additionally, events corresponding to the spatiospectral lobes occur intermittently and at different times from each other, leading to bursts of acoustic energy with rapidly changing directivities.

Nomenclature

c	=	speed of sound
D_j	=	fully expanded jet diameter
Sr	=	Strouhal number, fD_j/u_j
T	=	Markov transition matrix
u_j	=	fully expanded jet exit velocity
W_x	=	wavelet transform of signal x
$\|W_x\|^2$	=	wavelet power spectrum
x_e	=	event lipline location measured from the nozzle exit
θ	=	event propagation angle relative to the jet inlet
τ	=	cross-correlation time delay

I. Introduction

INTENSE sound levels produced by high-performance military jet aircraft can lead to hearing loss for launch personnel that are repeatedly exposed to these levels [1]. For this reason, it is desirable to characterize the noise generated by full-scale aircraft to further inform noise reduction efforts. These sound fields have been analyzed at full and lab scales as well as in numerical simulations. Unfortunately, sound fields predicted by numerical simulations and lab-scale measurements do not completely agree with those of full-scale tactical aircraft in terms of phenomena produced.

A key feature of high-performance military jet aircraft noise is multiple spatiospectral lobes, first identified by Wall et al. [2,3]. In their analysis, acoustical holography was used to create total-field reconstructions, and the lobes were characterized as distinct regions of high sound level that evolved through frequency. Before this work, the lobes were identified as a “dual-peak” phenomenon at individual microphone locations [4–6], in part because of limited spatial resolution and one-third octave band spectral analyses. However, the spatiospectral lobes can also be retroactively seen in other analyses. For example, in Stout et al.’s [7] vector intensity analysis (see included video), multiple lobes can be seen to form and evolve as frequency increases. An example of the spatiospectral lobes along a microphone array near the T-7A aircraft is presented at the top of Fig. 1. The color map shows levels at military power as a function of frequency (Strouhal number) and microphone position. Within the map are at least five regions of elevated level compared to the surrounding regions. These are the spatiospectral lobes. Four individual power spectral densities (PSDs) corresponding to microphones at 15, 20, 25, and 30 engine diameters (D_j) are included in the bottom of Fig. 1. These spectra show how the lobes appear for a single microphone. Vertical lines identify the spectral locations of the first four lobes, as in the top of the figure. Further details regarding the data in Fig. 1 are provided in Sec. III.

Several methods have been used to study these lobes. Harker et al. [5] performed preliminary correlation and coherence analysis, where they suggested that the dual-peaked spectra were created by multiple overlapping, incoherent sources in the jet. These conclusions were later expanded on by Swift et al. [8], who performed a related but more comprehensive analysis for the F-35. In their work, at least five individual spatiospectral lobes were identified in the peak-frequency region. They showed that coherence lengths increase within an individual lobe and decrease in regions of overlap between two or more lobes. Beyond standard signal processing of the field-acquired data, inverse methods have recently been largely employed to explore the apparent origin and other spatial behavior of the lobes. Wall et al. [3] used near-field acoustical holography (NAH) to recreate the sound field near a high-performance military aircraft. They then employed a partial field decomposition method to separate two lobes and showed that they result from multiple overlapping sources. Leete et al. [9] used NAH to track the F-35’s lobes through space and frequency. They determined that, as frequency increases, the lobes shift aft and eventually decrease in level while the next lobe appears at a steeper angle. (This behavior can also be seen in the vector intensity analysis of Stout et al. [7,10] for the F-22.) Leete et al.’s results were confirmed and expanded on for the T-7A by Olaveson et al. [11], using the hybrid beamforming method [12] and an improved ray-tracing method to determine apparent source locations for each lobe. Finally, for the T-7A, Mathews et al. [13] have used NAH to reveal a collection of overlapping local source maxima that appear related to the lobes.

Except for correlation, the above methods operate in the frequency domain, and inherent spectral averaging removes any temporal features. But to better understand the lobes’ underlying mechanisms, their temporal features must also be characterized. One such time-domain analysis has been developed in the form of event-based

---

Presented as Paper 2023-3213 at the 2023 AIAA Aviation 2023 Forum, San Diego, CA, and Online, June 12–16, 2023; received 11 January 2024; revision received 14 June 2024; accepted for publication 26 June 2024; published online 13 August 2024.

*Doctoral Candidate, Department of Physics and Astronomy. Student Member AIAA.

†Professor, Department of Physics and Astronomy. Associate Fellow AIAA.

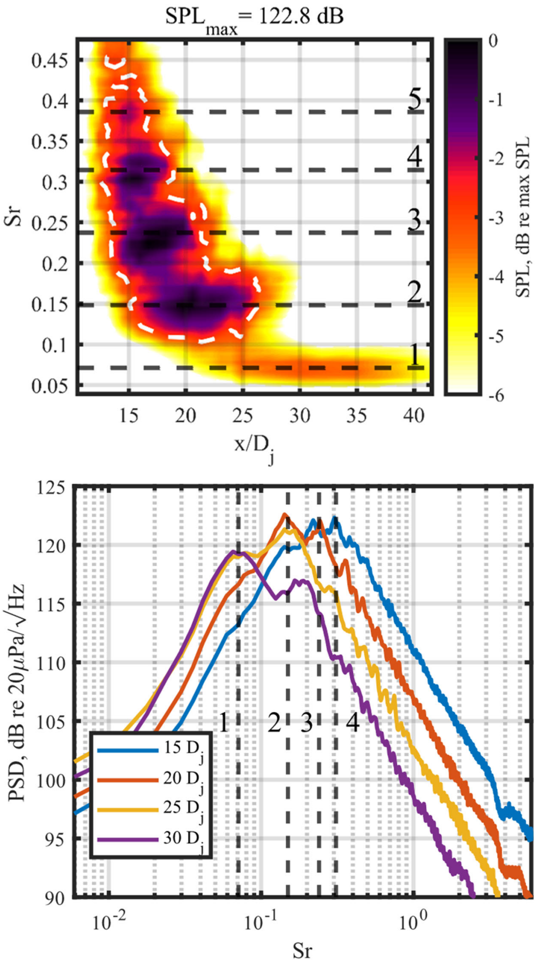

Fig. 1 Spatiospectral map at MIL (top). White contours indicate the 3-dB-down point. Four individual spectra (bottom) demonstrating the multi-lobed behavior.

beamforming (EBBF) by Vaughn et al. [14,15]. In their studies of jet crackle, they identified high-amplitude and high-derivative events in the time waveform and used cross-correlation between adjacent microphone pairs to beamform these events back to the jet lipline. The selected events and resultant distributions helped identify radiation and source characteristics of Mach waves and other known jet noise structures.

While each domain provides its own unique insights, a joint time–frequency domain (JTFD) analysis has the potential to connect features from both domains. The wavelet transform is a method of extracting frequency information at every time step in a signal [16] and has proven useful in identifying frequency events that change rapidly through time. In their analysis of a supersonic, lab-scale jet, Heeb et al. [17] used a wavelet transform to identify time-domain events corresponding to spectral tones related to screech modes. They then applied a time-domain analysis to further characterize the temporal distribution of these events. Kœnig et al. [18] used a wavelet transform to study temporal structures from a heated, subsonic lab-scale jet. In their work, the wavelet transform was used as a filter to extract time-domain features corresponding to peaks in the energy spectrum. From their analysis, they characterized a temporal intermittency associated with wavepackets and the impact of jet Mach number and temperature ratio on these features. Beyond these examples, a wavelet-based JTFD analysis has been used in jet noise to identify acoustic shocks [19], characterize waveform crackle content [20], and visualize Mach waves in conjunction with schlieren imaging [21].

A novel temporal approach is considered in this paper, in the form of Markov analysis. A Markov chain is a probabilistic model that describes the evolution of a single-state system with the condition that the next element in the sequence is only dependent on the current state. The result is a chain of states that encodes the model properties. These types of Markov models were first applied to letter content in poetry [22]. Other applications have been in communication and information theory [23], the response time of shared computational resources [24], gene identification in DNA strands [25], speech recognition [26], and Markov chain Monte Carlo methods [27].

Up to now, the lobes have been primarily identified as a spatiospectral phenomenon, but details on how the lobes manifest in the time domain have yet to be explored. The purpose of this paper is to analyze the spatiospectral lobes in combinations of the spatial, spectral, and temporal domains using the near-field noise generated by a T-7A-installed F404 engine. The final product is a spatiospectrotemporal representation of the lobes. First, a spatiotemporal analysis is performed using Vaughn et al.'s [14] EBBF algorithm in conjunction with the wavelet transform. Next, the temporal structure within the wavelet transform of microphone signals is analyzed using a Markov-style probability analysis to provide a lobe temporospectral characterization. Finally, the Markov model results are used to decompose measured spatiospectral maps into individual lobes to identify spatiospectral properties. These results are then summarized in an animation that represents the jet noise radiation and lobes in a spatiospectrotemporal sense.

II. Experiment

Data were collected from an F404 engine installed on a tethered T-7A trainer aircraft [28]. Six run-ups were performed by cycling through power settings ranging from idle to afterburner (AB). This paper focuses on the data collected at military power (MIL), i.e., 100% thrust. The measurement featured over 200 microphones arranged in multiple near-field arrays and far-field arcs with a microphone array reference point (MARP) located 3.96 m downstream of the nozzle. For this paper, only the 120-microphone, near-field imaging array is used, but other analyses have used the far-field arc (e.g., see [29]). This array was composed of GRAS 46BD and 46BG 1/4″ pressure mics recorded using NI® 24-bit data acquisition cards sampling at 204.8 kHz. Figure 2 shows a schematic of the imaging array setup. The array ran approximately parallel to the jet centerline in the forward direction and then transitioned to follow the anticipated shear layer downstream of the nozzle. A variable microphone spacing was chosen to appropriately resolve the expected peak frequency behavior in each region.

The MIL spectra along the array have been compiled into a spatiospectral map. To emphasize the spatiospectral lobe structure, the top of Fig. 1 shows only the top 6 dB of this map with a 3-dB-down contour in white. At least five spatiospectral lobes are present in the figure, which is consistent with previous observations on the F-35 [9]. Unlike previous analyses on full-scale aircraft, spectral results in this paper are presented in terms of Strouhal number with $Sr = fD_j/u_j$, where D_j and u_j are the fully expanded jet diameter and exit velocities, respectively. The lobes have a spectral spread, but for this paper, they will be identified by a single frequency that corresponds to the approximate spectral center of each lobe. The first occurs at a Strouhal number of ~0.071 and beyond 25 D_j. The higher-ordered lobes (2+) appear as dark patches near Strouhal numbers of 0.15, 0.24, 0.31, and 0.39, respectively, and shift upstream from ~20 D_j to ~15 D_j with increasing lobe number. These Strouhal

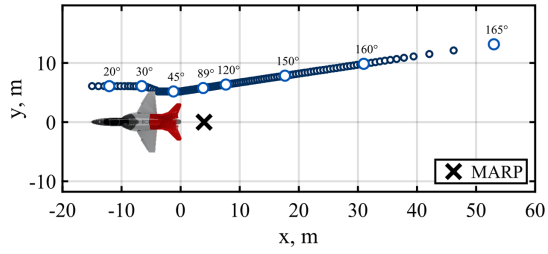

Fig. 2 T-7A A measurement schematic.

numbers are quasi-harmonic, and a similar structure was seen in F-35 noise measurements [8].

III. Methods

A. Event-Based Beamforming

EBBF identifies apparent locations and propagation angles of time-domain events. First, an event type is defined. Historically, these have been either large pressure amplitudes or large derivatives [14,15], though any time-domain structure is viable. For each pair of adjacent microphones, the top N most prominent events are identified in the upstream microphone's time signal with a minimum separation, δt, between each event. The choice of N can impact the EBBF performance. If N is too large, nonphysical events will be identified in the underlying noise, but if N is too small, there are fewer data points for averaging. The time separation is included to prevent events from being double-counted and to ensure a broader sampling of the waveform.

For each event, a Hann window is applied to the waveform centered on the event. A similar window is applied to the downstream signal, isolating the event in each waveform. The cross-correlation of the two windowed signals is then used to calculate a time delay, τ, between the two events. Using the time delay, a sound speed of $c = 343$ m/s, and the assumption that the event is locally planar in the region of the microphones, identifying the apparent propagation angle and lipline source location reduces to a geometry problem. Figure 3 depicts the EBBF geometry, with the T-7A measurement schematic presented as a 3D model. The aircraft is in the upper left corner, and the microphone array is to the right, shown as blue circles. The vector $\boldsymbol{r}_m$ points from the upstream to the downstream microphone and has a length equal to the distance between the two, though it has been exaggerated here. The vector $\boldsymbol{r}_s$ traces the linear event path and points from the microphone midpoint to the jet lipline. Following the same formulation as Vaughn et al. [15], the event propagation angle is

$$\theta = 180^\circ - (\phi + \alpha) \tag{1}$$

where $\alpha = \tan^{-1}(\Delta y/\Delta x)$ is the angle formed from the microphone geometry and $\phi = \cos^{-1}(c\tau/d)$ is the angle between $\boldsymbol{r}_m$ and $\boldsymbol{r}_s$. The apparent event source location is extracted from the inner product:

$$\boldsymbol{r}_m \cdot \boldsymbol{r}_s = |\boldsymbol{r}_m||\boldsymbol{r}_s|\cos\phi \tag{2}$$

The event is assumed to come from the lipline location $r_s = \langle x_e, D_j/2, h\rangle$, where h is the nozzle centerline height and x_e is the unknown event origin relative to the nozzle. Equation (2) is then solved for x_e. This ray-tracing procedure is performed for each of the N events and each microphone pair.

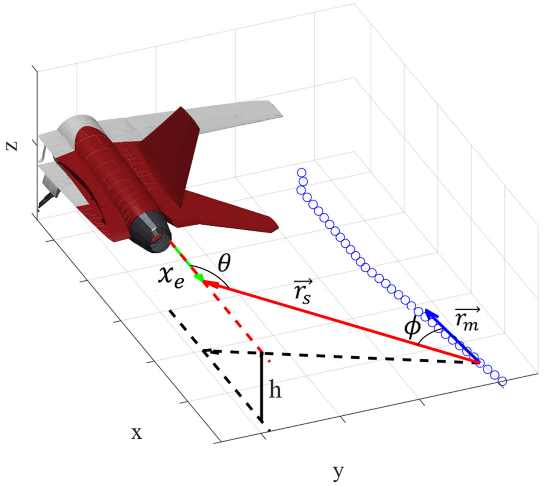

Fig. 3 Event-based beamforming geometry. The vector $\boldsymbol{r}_m$ points from the downstream to the upstream microphone, $\boldsymbol{r}_s$ from the downstream microphone to the (unknown) event location, and $\boldsymbol{x}_e$ from the nozzle to the event.

B. Wavelet Transform

Whereas the EBBF procedure was developed for the time domain, examining the spatiospectral lobe behavior in detail requires frequency information as a function of time. The short-time Fourier transform can provide this information, but the uncertainty principle dictates that increasing the time resolution necessarily reduces the frequency resolution [30]. A balance between the two can be attempted, but the EBBF algorithm requires a high time resolution. Even with a time step of 20 ms, the error surpasses what is reasonable. A different method is required to appropriately balance frequency and time resolutions.

The wavelet transform extracts frequency information at every instant in time [16]. The basic formulation involves repeatedly convolving a time signal, x, with a wavelet, ψ, that is scaled to match a specific frequency of interest. This is typically written as $P(s,t) = \int x(t)\psi(\tau/s)\,\mathrm{d}\tau$ where s indicates the wavelet scale. The scaling factor is then converted to frequency, which results in a complex function that describes the temporospectral behavior of the signal. The magnitude and phase information can be analyzed individually [21], or together as a wavelet power spectrum $|W_x|^2$ [16]. When viewed as a power spectrum, $|W_x|^2$ is a scalogram that depicts frequency-dependent energy content through time. While many families of wavelets exist, this paper uses the Morlet wavelet, which evenly balances temporal and spectral resolution. The Morlet wavelet is a complex Gaussian expressed as $\psi(t) = e^{-t^2/2}e^{j5t}$, which is the MATLAB default. Other families were investigated, but the results presented here do not change significantly with wavelet type. Figure 4 shows an example of a 50 ms waveform (top) and the corresponding wavelet power spectrum (bottom) from a microphone located at $x = 18.9\ D_j$. This signal contains shocks, which appear in $|W_x|^2$ as faint vertical stripes of high-frequency content at the shock location [20]. Additionally, there are two high-amplitude events at relatively low Strouhal numbers: 15 ms at $Sr = 0.24$ and 27 ms at $Sr = 0.15$. These Strouhal numbers correspond to the spatiospectral lobes at this location and form prominent peaks in the time-averaged Fourier spectrum.

This paper uses the wavelet transform to identify frequency events in the time signal for use in EBBF by searching for peaks in time slices of $|W_x|^2$ at the lobe Strouhal numbers, i.e., $|W_x(Sr_i,t)|^2$.

C. Markov Chains

Temporospectral events like those seen in Fig. 4 are observed in a majority of $|W_x|^2$ snapshots for microphones where the lobes are present. These events occur intermittently and exhibit a visual frequency-switching phenomenon. Qualitatively, the events appear as discrete bursts or puffs of energy, which is similar to the temporal behavior of wavepackets [31,32]. This same behavior has been observed in lab-scale experiments and numerical simulations of subsonic jets [18,33–35]. However, the events in Fig. 4 occur at alternating frequencies, which resembles the screech tone mode switching in lab-scale jets [17]. Since the events occur intermittently and at different frequencies, wavelet transform time slices are

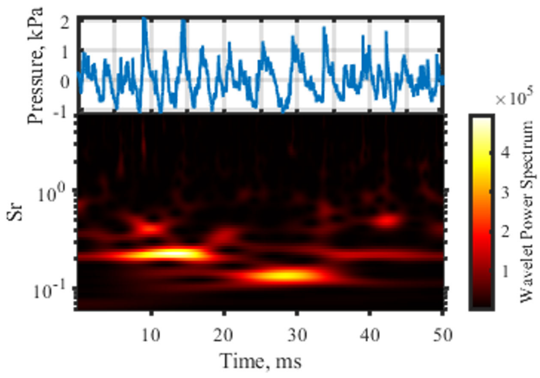

Fig. 4 A 50 ms waveform (top) and corresponding wavelet transform (bottom). Spectral events are seen as bright islands in the transform.

nonstationary signals, and classic Fourier analysis struggles to meaningfully quantify the behavior. While other methods have been developed to circumvent similar issues, for example, Kearney-Fischer et al. [36], this paper models the events as a Markov process.

There are two components to the Markov model: the transition matrix and state sequence. The transition matrix is a row-normalized, square matrix with entries T_{ij} that gives the probability of transitioning from one state, s_i, to another, s_j, after a time step. The state sequence, S, is generated from the transition matrix by defining S_1 and choosing the next state (and each subsequent one) based on the probabilities in T. Sometimes T is unknown, but S is provided or measured. By assuming that S is a Markovian process, T can be calculated empirically by determining the transition probabilities from the sequence itself. Thus, any underlying structure in the state sequence is modeled by the transition matrix. This matrix can be used to predict the future state of a sequence by taking repeated powers of T, where $(T^n)_{ij}$ is the probability of transitioning from s_i to s_j on the nth step. In the limit as n goes to infinity, the rows of T^n become identical, and each contains the steady-state solution, which shows the long-term prevalence of each state in S.

This paper models the frequency-switching phenomenon in Fig. 4 as a Markov process and explores the probabilistic relationship between events at the lobe center frequencies. The state sequences for each microphone are then used to develop an event-based spectral decomposition that breaks down the time-averaged Fourier spectrum into individual spectra for each spatiospectral lobe.

IV. Analysis

This section characterizes the spatiospectral lobes in three combinations of the time, space, and frequency domains. A spatiotemporal analysis combines the wavelet transform with EBBF to target frequency events corresponding to each spatiospectral lobe. The temporospectral events seen in the wavelet transform are then modeled as a Markov chain and the underlying structure is discussed. From the Markov model, the time-averaged Fourier spectrum is decomposed by taking ensemble averages of events corresponding to each lobe individually. This process is then applied to the entire microphone array to create new spatiospectral maps for each lobe. Finally, all these results are combined into a single spatiospectrotemporal animation that depicts the overall behavior of the spatiospectral lobes.

A. Event-Based Beamforming with Wavelets: Spatiotemporal

EBBF has been used elsewhere to characterize crackle-related events [14], and the method is now used to explore the lobe's spatiotemporal properties. Since the lobes are inherently spectral phenomena, EBBF requires a frequency trigger. The trigger uses prominent local maxima in time slices of the wavelet power spectrum, $|W_x(Sr_i, t)|^2$, where Sr_i is a characteristic Strouhal number for a given lobe. This translates to beamforming at time locations where the measured signal has a relatively large amount of energy at the desired Strouhal number, or lobe. This paper uses $N = 500$ events and a minimum event separation time of $\delta t = 2.4$ ms. The number of events was chosen through a trial-and-error process similar to Vaughn et al. [15], with 500 events representing a large enough number without oversampling the natural noise in the signal. A 2.4 ms event separation was chosen to allow enough space between events to avoid double counting.

Since only a subset of the imaging array shows evidence of the spatiospectral lobes, only the affected range of microphones is used in the beamforming. The same procedure could be applied to the rest of the array, but events outside this range are low amplitude and irrelevant to the spatiospectral lobes. Using Fig. 1 as a guide, the relative spatial regions are presented in Table 1 for each lobe. The spectral characteristics of the lobes shift with position, but only a single Strouhal number is chosen to characterize the lobes since the event triggers are only defined for a single frequency at a time. The spatial ranges presented here are generous enough to capture the 3-dB-down point around each lobe and a little bit more. Once the EBBF algorithm is applied to these microphone regions and Strouhal numbers, the resultant propagation angles and apparent lipline source locations for each lobe are compiled into normalized histograms.

Table 1 Approximate spatiospectral regions corresponding to each lobe as seen in Fig. 1

Lobe	Strouhal number	Spatial range, D_j
1	0.071	$24 \le x_m \le 39$
2	0.15	$15 \le x_m \le 26$
3	0.24	$13 \le x_m \le 21$
4	0.31	$13 \le x_m \le 17$
5	0.39	$13 \le x_m \le 17$

Figure 5 shows the angle and intercept histograms as a function of microphone location for each spatiospectral lobe. The probability of each event is calculated as the number of events that fall into that bin, divided by the total number of events. These probabilities are

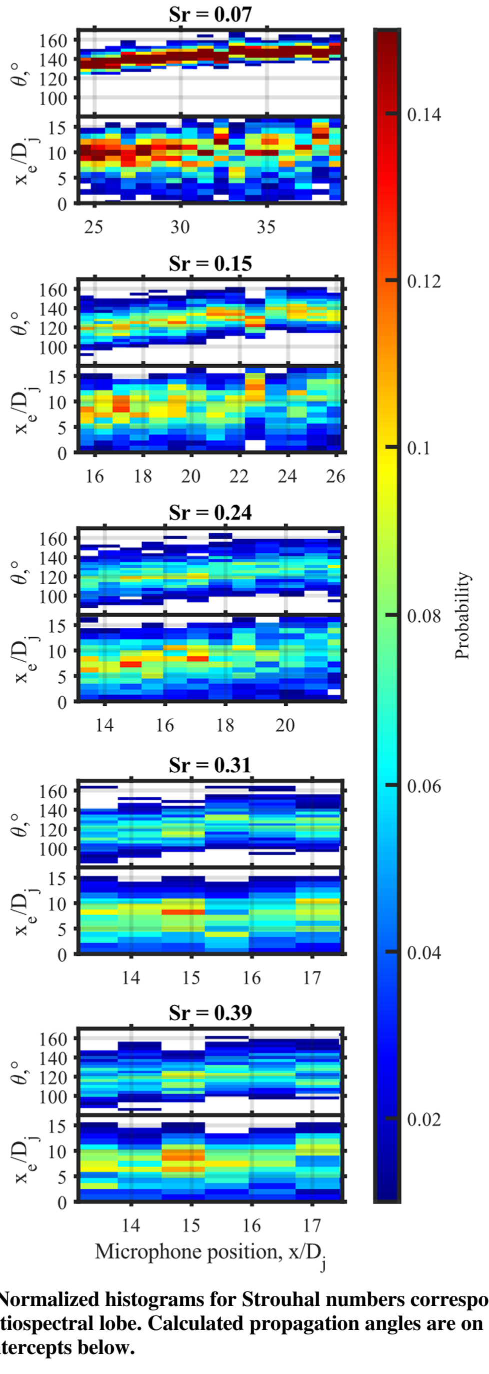

Fig. 5 Normalized histograms for Strouhal numbers corresponding to each spatiospectral lobe. Calculated propagation angles are on top with lipline intercepts below.

indicated by color, with values below 0.01 set to white to highlight the relevant trends. For the higher-ordered lobes, especially lobes 4 and 5, there are relatively few microphones within the lobe's spatial extent, causing these figures to appear slightly blurred. The propagation angle histograms (top) indicate that the events responsible for each lobe have a relatively steady propagation angle, although with a slight upward trend with increasing microphone position, suggesting that events must propagate at steeper angles to reach the farther microphones. The intercept histograms (bottom) also exhibit this upward trend, though with enough spread to remain relatively constant.

The angular distributions and event source locations are summarized in Table 2. For each microphone in the aperture, the mean and standard deviation of the radiation angle (and event origin) are calculated. An overall mean is obtained by averaging the means across all microphones. The overall minima and maxima are determined from the highest and lowest values that are one standard deviation away from their respective means. In this way, the ranges presented in Table 2 capture all the primary distribution information as well as some tapering at either end.

The table contains two key results. First, the average radiation angle decreases as the lobe number increases. Lobe 1 radiates at around 141°, and each subsequent lobe radiates farther to the sideline, with lobe 5 being about 121°. Additionally, there is a strong angular overlap between lobes 2–5, with the mean angle for lobe 5 being captured by the range of lobe 2 and vice versa. There is very little angular overlap between lobe 1 and the others. The second result of interest is the contraction and overlap of the apparent source regions. Lobe 1 is predicted to occur at about 8.4 D_j, and each subsequent lobe is seen to move closer to the nozzle, with lobe 5 coming from around 6.4 D_j. This behavior matches what is expected from the developing jet turbulence. Closer to the nozzle, the turbulent length scale is relatively small, resulting in high-frequency radiation. Further downstream, the developing turbulence grows in size and thus radiates at a lower frequency. Finally, the spatial ranges associated with each lobe monotonically decrease as the lobe number increases. The range width starts at about 8 D_j for lobe 1 and ends with a range of about 5 D_j for lobe 5. The observation that source regions contract and move upstream with frequency is consistent with jet noise literature (see, e.g., Refs. [7,37]), but expands this from the statistically averaged domain to individual time events.

These results compare favorably with those predicted by Olaveson et al. [11]. From their ray tracing analysis of steady-state lobe behavior reconstructed from hybrid beamforming, they predicted radiation angles for MIL of about 140° for lobe 1, 128° for lobe 2, 125° for lobe 3, and 120° for lobe 4. Due to the limited resolution of their ray-tracing method, they were unable to make predictions for lobe 5. Spatially, the beamforming suggested that lobe 1 occurs downstream of the supersonic core tip (~13 D_j). Lobe 2 was predicted to occur between the potential and supersonic core tips, with lobes 3 and 4 moving upstream and clustering upstream of the potential core tip (~7 D_j). Aside from lobe 1, the EBBF results are similar. Lobe 2 spatially falls between the two core tips, and the higher-order lobes move steadily upstream before resting just near the supersonic core tip.

Table 2 Predicted radiation angles and event source regions for each lobe as calculated from the data in Fig. 5

	Radiation angle ($\theta°$)			Source location (x_e), D_j		
Lobe	Min	Mean	Max	Min	Mean	Max
1	131	141	149	4.8	8.4	12.9
2	115	127	140	4.9	7.7	11.7
3	113	122	132	4.3	7.1	10.9
4	113	122	128	3.8	6.5	9.0
5	112	121	128	4.1	6.4	8.8

While the histograms in Fig. 5 and numerical results in Table 2 provide the EBBF results, it is difficult to connect the relationships between the event source location and radiation angle. The results are now presented as a collection of ray-traced events to better visualize this connection. For each microphone pair, the mean of the corresponding propagation angle distribution is used to linearly trace the "average" event back to the jet lipline. Figure 6 shows this process applied to each lobe Strouhal number. Microphones are represented as blue dots, and the jet lipline is shown as a dashed line. The ray-traced events are shown as different colored lines. Included below the lipline is a similarly colored bar that spans the apparent source region from Table 2 with a black "x" at the mean value. It is visually apparent that the sources corresponding to each lobe gradually move upstream, but each has significant overlap with the other lobes. The radiation angles also exhibit overlap and steepening with increasing lobe number.

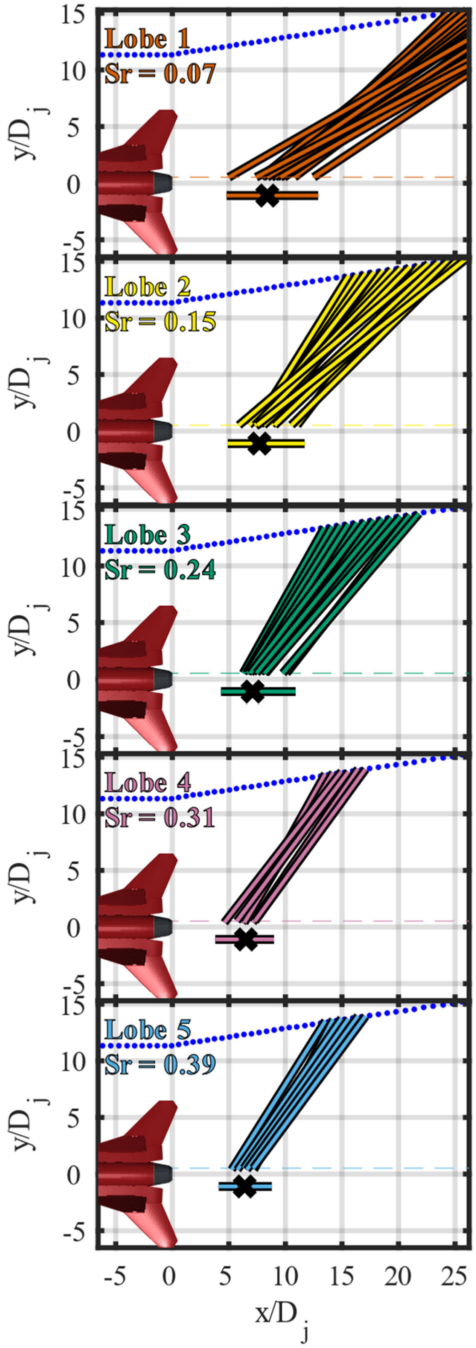

Fig. 6 Average event path predicted using the mean propagation angle for each microphone pair.[1‡]

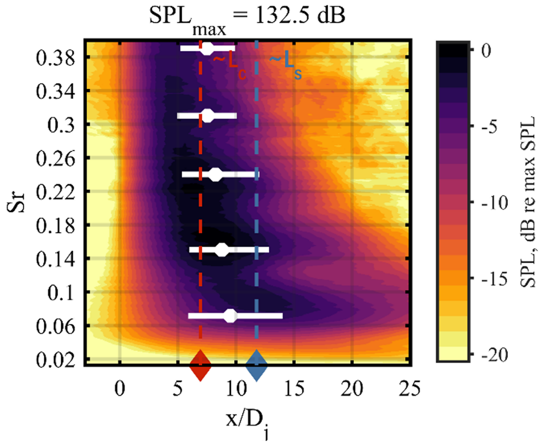

Fig. 7 EBBF source locations compared to acoustical holography results.

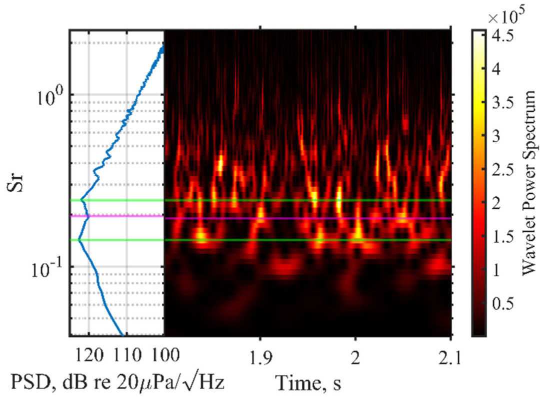

Fig. 8 Power spectral density (left) of the full 30 s waveform from Fig. 4 with a double peak and a 0.3 s wavelet transform snapshot (right). Spectral extrema are highlighted in green and magenta.

The predicted event source locations corresponding to each lobe are now compared with predictions made using NAH performed by Mathews et al. [38], who used the same dataset as in this paper. In their analysis, the source was represented by an acoustic field reconstruction at the jet lipline. Figure 7 shows their spatiospectral source reconstruction for MIL, which exhibits a collection of local maxima (LM) that may be related to the spatiospectral lobes. Vertical dashed lines identify the spatial locations of the assumed potential (red) and supersonic (blue) core tips. To compare the time-averaged holography analysis and the EBBF results, the predicted source regions from Table 2 are added to the plot as white horizontal lines with the mean value as a white dot. The EBBF source predictions for each lobe neatly coincide with one of the LM at the same Strouhal number. The implication is that each of the LM can be connected to one of the lobes—all except the first.

For lobe 1, there is very little overlap between the EBBF predictions and the lowest LM. The mismatch between lobe 1 and the lowest LM suggests that lobe 1 does not behave in the same way as the higher-ordered lobes, or perhaps these two methods are identifying different, unrelated phenomena. A similar disagreement is also seen when compared with the beamforming results. Vaughn et al. [14] used the same EBBF method to characterize source locations of acoustic phenomena on the F-35. When lobe 1 is compared to their results (see their Table 1 and Fig. 10), the source region occurs at the overlap between groups 4 and 5. These groups represent the transition from Mach wave radiation to large-scale turbulent structure noise. In relation to the flow, this indicates a transition from supersonic to subsonic convection of the turbulence. That the lower frequencies should occur in this subsonic regime is consistent with the literature. Holography and beamforming predict source locations farther downstream, which suggests that lobe 1 is primarily composed of large-scale structure noise. Since EBBF uses high-amplitude frequency event triggers, most events will be related to the Mach waves pushing the predicted source region closer to Vaughn's group 4. This is also consistent with Leete et al.'s [9] suggestion that lobe 1 is a superposition of multiple lobes or phenomena. When compared against the other lobes, lobe 1 has a Strouhal number of about 0.07, which roughly corresponds to the difference frequency between lobes 3 and 4. There is also significant overlap between the corresponding source regions for these lobes. These two observations point toward a possible nonlinear interaction between the higher-ordered lobes. Future work will explore possible nonlinear interactions between the spatiospectral lobes.

B. Markov-Style Event Characterization: Temporospectral

The events described in the previous sections are seen to occur intermittently with a possible relation between lobe frequencies. This section applies a Markov-style analysis to the full 30 s waveform from Fig. 4 to characterize the event temporal structure. Figure 8 shows the PSD (left) using a frequency bin size of 10 Hz ($\Delta Sr \approx 0.005$). This waveform captures radiation at about 144° and exhibits multilobed behavior, which is evidenced by the two notable spectral peaks at $Sr = 0.14$ and $Sr = 0.24$ corresponding to lobes 2 and 3, respectively. The right of Fig. 8 shows $|W_x|^2$ for a 0.3 s portion of the waveform. Included in the figure are three horizontal lines. The green lines highlight the power spectral peaks, while the magenta line shows the central dip. Most temporospectral events coincide with one of the peak frequencies, though many smaller events appear at minor spectral peaks. Additionally, several events appear at the spectral dip. This is unsurprising. Even though this dip is a local minimum, it still has a higher level than the rest of the spectrum.

Between this snapshot and others, events are seen to oscillate between spectral peaks. This behavior is most notable near 1.95 s, where four events bounce between the two green lines and then a fifth lands on the magenta line. This oscillatory behavior is not periodic, and neither is the spacing between groups of events. Moreover, whenever there is an event at one of these peak frequencies, there tends to be a relative minimum at the other peak. A preliminary correlation analysis is performed on the wavelet time-slices at $Sr = 0.14$ and $Sr = 0.24$ to determine a characteristic spacing between events. Each signal is divided into one hundred 0.3 s blocks (as in Fig. 8) to ensure that multiple events are present in each block. The cross-correlation between each signal is then calculated, and the time lag corresponding to the maximum correlation coefficient is extracted. Despite this, no "characteristic" time scale is recovered, although the distribution is somewhat Gaussian and centered on zero. A different method of characterizing the relationship between events is thus required.

Since the events' timing and duration are intermittent, classical Fourier analysis struggles to extract meaningful information. Additionally, the sporadic behavior of the events makes investigating temporal relationships between the lobes challenging. For this reason, a Markov-style analysis is used to model temporal behavior. To create the Markov model for this behavior, the measured time signal is represented by a state sequence. States are defined as s_{00} for no events, s_{01} for an event at $Sr = 0.24$, s_{10} for an event at $Sr = 0.14$, and s_{11} for an event at both Strouhal numbers. While additional peaks are present (lobe 4 appears at $Sr \approx 0.35$), only events at these Strouhal numbers are considered for simplicity. The state sequence is created as follows.

First, the $|W_x(0.14, t)|^2$ time slice is extracted from the wavelet transform and divided into six thousand 5 ms blocks. This step size was chosen to match the observation that many events have an estimated duration of about 10 ms. Many have longer or shorter durations, but an exact value is unnecessary so long as the Markov chain step size is smaller than the typical event. Using a smaller step size produces the same results and is used in Sec. IV.C, but it is difficult to interpret a matrix whose off-diagonals are vanishingly

---

[‡]Lobe colors have been changed from how they were initially presented in Ref. [11]. The updated colors are now orange, yellow, green, purple, and blue for lobes 1–5.

small. Once the wavelet time slice has been divided into blocks, the mean value of each block is compared to half the mean square value of the measured signal. If the block mean is larger, then that time sample is marked as having an event at $Sr = 0.14$. The same procedure is then repeated for $Sr = 0.24$. Olaveson et al. [39] compared block means to the root mean square (RMS) level of each wavelet slice instead of using the overall signal. This updated method does not change the conclusions presented in that preliminary work, but it does improve the ability to characterize events across the entire microphone array. Once both sequences of events have been created, each sample is compared, and a final state sequence is compiled by sorting the resulting combinations into the appropriate states.

Once the state sequence is defined, MATLAB's *hmmestimate* function is used to fill out the transition matrix. These values are presented in Table 3. The table can be read by starting at any of the four states in the left-hand column, and then the probability of transitioning to any of the other states is found by locating the column corresponding to the desired state. Included in the last row of the table are the average event lengths and steady-state solution. The matrix shows that there are relatively high probabilities of transitioning from any state into s_{00}, indicating that most of the signal is dominated by having no events at either Strouhal number. On the contrary, the lowest probabilities in the matrix are seen to be transitions into s_{11}. Thus, when the sequence transitions from an event at one spectral peak to another, it prefers to fade out one event before introducing the next one rather than overlapping the two. This same behavior extends to interactions between events when more than two lobes are present. While one lobe radiates, the system prefers to fade out that lobe before starting a new one. In the rare case where multiple lobes radiate simultaneously, changes in which lobes radiate tend to follow a "switch off/switch on" procedure.

Overlap between events will depend on their typical durations, which can be calculated from the weighted sum $\overline{L} = \Delta t \sum_{n=0}^{\infty} nP(n)$, where n is an integer and $P(n)$ is the probability of a sequence of that length occurring. The factor of Δt is included to convert from steps to seconds. For the states $s_i \in \{s_{00}, s_{11}\}$, the calculation is straightforward:

$$\overline{L}_i = \Delta t \sum_{n=0}^{\infty} nT_{ii}^{n-1}(1 - T_{ii}) \tag{3}$$

where subscripts on T indicate the matrix index for that state. The probability assumes that the system starts in the desired states and remains there for $n - 1$ steps before finally transitioning to a different state. This process returns chain lengths of $\overline{L}_{00} = 20$ ms and $\overline{L}_{11} = 6.1$ ms. The process for the states $s_i \in \{s_{01}, s_{10}\}$ is complicated slightly by the presence of s_{11}. Since the chain can begin in either s_i or s_{11} and can have any number of transitions between these states before leaving, the probability needs to account for every combination of paths. It is simpler to recreate the state sequence by making the substitutions $s_{11} \to s_i$ and $s_{j \neq i} \to s_{00}$, which reduces the transition matrix to a 2×2. Equation (3) then applies. This computation returns the chain lengths of $\overline{L}_{01} = 8.4$ ms and $\overline{L}_{10} = 9.8$ ms. Converting these values from milliseconds to periods yields 2.4 and 3.4 periods, respectively. These results suggest that when an event appears in the signal, it remains for only a few cycles before fading out. Additionally, long breaks tend to separate chains of events, which qualitatively matches the visually observed temporal intermittency. Finally, the fact that $\overline{L}_{11}$ is less than either $\overline{L}_{01}$ or $\overline{L}_{10}$ implies that when events do overlap, it is more likely that one event is fading out while the next comes in rather than two events starting at the same time. These overlaps are uncommon, as is shown by the steady-state solution.

Table 3 Transition matrix for the state sequence

From / To	s_{00}	s_{01}	s_{10}	s_{11}
s_{00}	0.75	0.17	0.059	0.022
s_{01}	0.51	0.37	0.072	0.051
s_{10}	0.41	0.11	0.40	0.088
s_{11}	0.27	0.23	0.32	0.18
Event length, ms	20	8.4	9.8	6.1
Steady state	0.64	0.21	0.11	0.042

Each element represents the probability of making a state transition (from row to column) at each time step. S_{00} is no events, S_{01} is an event at $Sr = 0.24$, S_{10} is an event at $Sr = 0.14$, and S_{11} is an event at both Strouhal numbers.

The steady-state solution is included beneath the transition matrix in Table 3 and represents the long-term content of the system. From these values, it is seen that the noise signal spends most of its time without events at either peak frequency. More interesting is the relationship between the states and events. By comparing the steady states for s_{01}, s_{10}, and s_{11}, it is seen that an event is 7.5 times more likely to occur at one peak at a time rather than both simultaneously. Combining this with the analysis from Sec. IV.A paints the picture of a time signal that is characterized by short, intermittent bursts of energy at spectrally important Strouhal numbers. The events radiate at different directivities, last only a few wavelengths, and then fade away, leading to an acoustic "flapping" phenomenon. These results also show that the turbulent events corresponding to the spatiospectral lobes occur at different times and that their superposition is an effect of the usual time-averaged methods like holography and beamforming.

To confirm the significance of the Markov analysis, this same process has also been applied to pure white noise and to white noise filtered to have the same spectral shape as in Fig. 8. As expected, the pure white noise is devoid of spectral events leading to a model with only a single state: s_{00}. For the shaped white noise, the results closely match what is seen in Table 3, suggesting that the distribution of events is primarily dependent on the signal's spectral shape.

C. Event-Based Spectral Decomposition: Spatiospectral

Now that the lobes have been characterized temporally, the next step is to observe the spatiospectral properties of individual lobes. This section uses the Markov state sequence to extract and combine spectra for individual lobes.

The process is demonstrated on a single microphone and then applied to the entire microphone array, leading to an event-based spatiospectral decomposition.

To begin, a new state sequence is generated using the same procedure outlined in Sec. IV.B, except that every sample of the waveform is used instead of dividing it into blocks. Using the new state sequence as a guide, the spectrum for each event is extracted from $|W_x|^2$. The average PSD corresponding to s_i is then calculated as

$$\mathrm{PSD}_i = \frac{1}{N} \sum_{n=1}^{N} |W_x(Sr_i, t_n)|^2 \tag{4}$$

where N is the number of times the state appears in the sequence and t_n is the time location of the nth occurrence of the state. These curves are plotted in Fig. 9 along with the Fourier spectrum (G_{xx}) and the averaged wavelet power spectrum. The mean wavelet spectrum closely matches the Fourier spectrum, although with some smoothing caused by the spectral response of the Morlet wavelet. The single-state spectra show that when events occur at one spectral peak, there is a reduction of energy at the other peak, indicating that these lobes are, in general, temporally separable and spectrally unrelated.

Since the Markov model is not limited to two Strouhal numbers, this same analysis can be applied to any number of spectral peaks. Using a spatiospectral map covering the span of the microphone array as a guide, spectral peaks corresponding to the spatiospectral lobes are identified in each microphone spectrum. Figure 10 shows a spatiospectral map with five sets of colored markers. Each marker is a spatiospectral coordinate that follows one of the lobes as it evolves through space and frequency and indicates the Strouhal numbers that the Markov model will characterize. The markers extend spatially beyond the darkest regions of each lobe to demonstrate the spatiospectral tapering of each lobe as it fades.

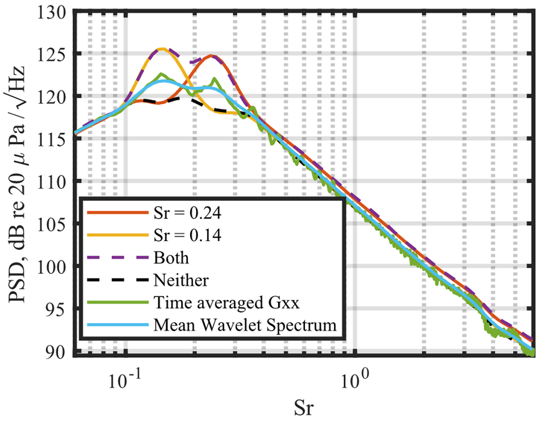

Fig. 9 Event-based spectral decomposition using events from the wavelet transform and state assignment from the Markov chain.

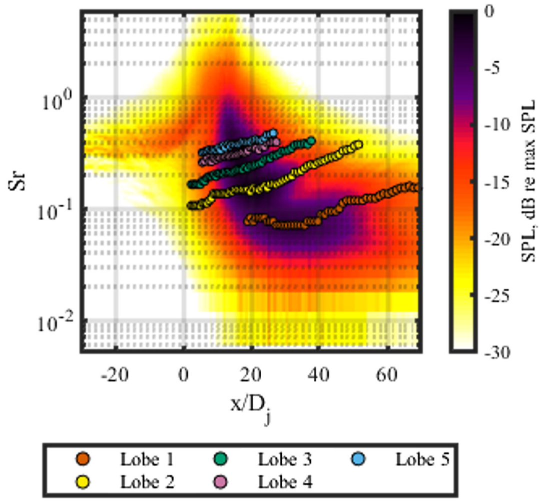

Fig. 10 Strouhal numbers by microphone position for each of the five lobes.

The Markov-style analysis is now applied to the entire microphone array. For n spectral peaks, the available states include every combination of events and nonevents at each Strouhal number. As an example, if there are three spectral peaks, $[Sr_1, Sr_2, Sr_3]$, then the set of available states is given by s_{ijk} where subscripts i, j, and k represent one of the Strouhal numbers and $ijk \in \{000, 001, 010, 011, 100, 101, 110, 111\}$. A value of 1 indicates an event at that Strouhal number, and zero indicates no event. The state s_{101} represents an event at Sr_1 and Sr_3 but no event at Sr_2. Performing the Markov-style analysis for this set of Strouhal numbers would produce an 8×8 transition matrix. Equation (5) is then used to calculate the spectrum for each state.

To collectively represent the spectra of individual lobes, overlap between relevant states needs to be accounted for. The overlap is calculated by taking a weighted average of the spectra for each state that has an event at the lobe Strouhal number with weights given by the steady-state solution. The spectra are then plotted together to form a spatiospectral map and normalized relative to the maximum value. Figure 11 shows the event-based spatiospectral decomposition with microphone position (in D_j) on the abscissa, Strouhal number on the ordinate, and level in color. A white contour marks the 3 dB-down point in each plot. Each subfigure shows the spatiospectral spread of each lobe as extracted from the time-domain signal. For the higher-ordered lobes, especially 3–5, a large vertical smear is present around the primary maximum. This smear is caused by overlapping temporospectral events in the wavelet transform and implies an overlap of temporospectral properties of the lobes.

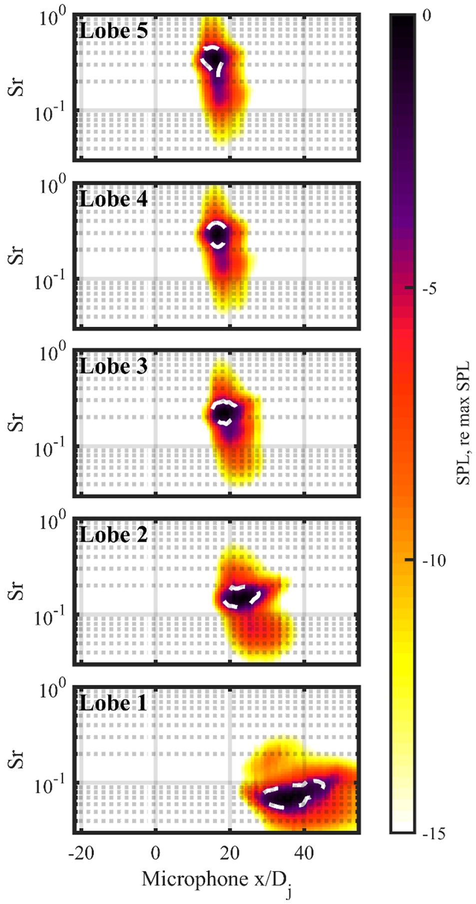

Fig. 11 Event-based spectral decomposition applied to the entire microphone array with a white contour at the 3-dB-down point.

Comparing this result to the overlapping sources in Fig. 6 confirms a strong relationship between the higher-ordered lobes. Lobe 2 deviates slightly from this pattern in that the downstream protrusion becomes clearer, and there is only a weak overlap with lobe 1, which is again consistent with the observation that lobe 1 does not act the same as the other lobes. The lack of strong overlap suggests that the source responsible for lobe 2 is not strongly coupled to the other lobes. It is concluded that events for each lobe occur intermittently with minimal overlap between lower-ordered lobes and increasing overlap as the lobe number rises.

D. Spatiospectrotemporal Lobes

This work has analyzed the lobes in combinations of the different domains. These have been space-time (spatiotemporal) from the wavelet-enhanced EBBF, time-frequency (temporospectral) from the Markov-style analysis of the wavelet transform, and finally space-frequency (spatiospectral) in the event-based spectral decompositions. Using the three represented domains, the lobes can now be considered as a spatiospectrotemporal phenomenon. Combining the observations from all analyses has led to the conclusion that the spatiospectral lobes are created by characteristic spectral events occurring in the measured waveform. These events appear to radiate from overlapping sources near and upstream of the potential core tip with different directivities associated with each lobe. Additionally, events corresponding to each lobe are independent of each other but statistically prefer to occur at different instances in time. To better present this conclusion, the results are combined into a single-time animation. The full animation is included as multimedia in the supplementary material, but select time snapshots are presented in Fig. 12. Many features of the plots have been removed in the interest of presenting multiple snapshots within a reasonable amount of space. Events corresponding to each spatiospectral lobe follow the same color convention that has been used throughout this paper:

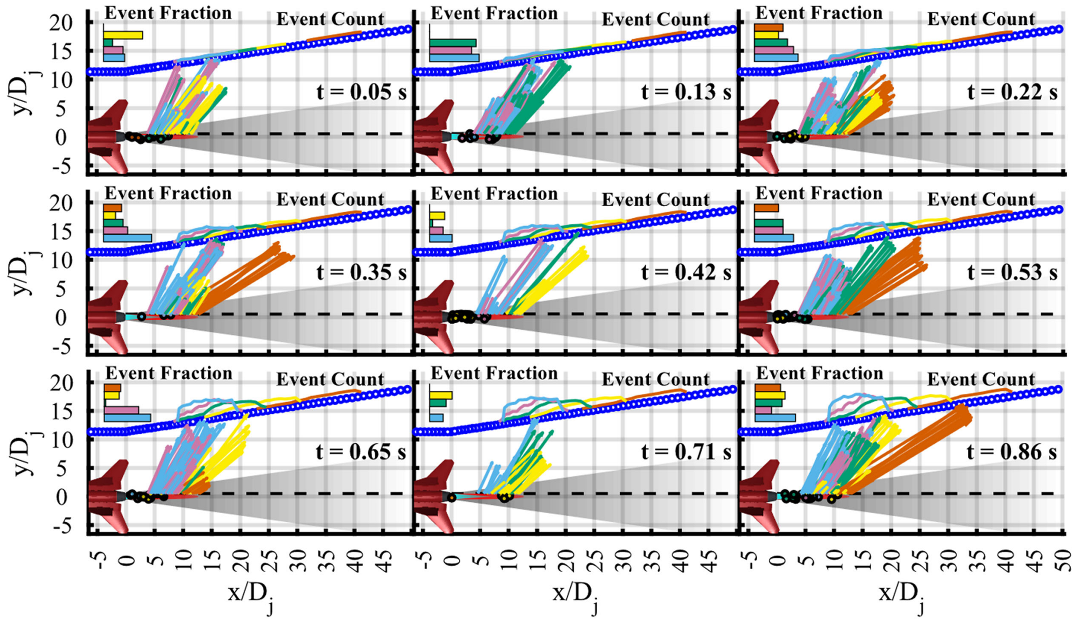

Fig. 12 Select snapshots from the supplemental animation.

orange, yellow, green, purple, and blue for lobes 1–5. The snapshots in Fig. 12 are chosen to illustrate some of the typical lobe behavior. As time progresses, the intermittency of each lobe is seen in that there is at least one frame where there are no events. The exception is lobe 5, which is discussed in the following paragraphs. Additionally, there is not a single lobe that consistently dominates the others at all times, and each lobe is the most prominent at one point, as is seen by the “Event Fraction” bars in the top left corners.

The animation combines results from each of the preceding analyses. First, the wavelet power time signals corresponding to each spatiospectral lobe, $|W_x(Sr_i, t)|^2$, are calculated for each microphone in the imaging array. Next, the most prominent peaks in each waveform are located as in EBBF. Of these peaks, only those that have a level greater than half the RMS level of the signal are kept as events, consistent with event identification for the Markov analysis. This means that microphones are not preselected to have specific lobes and allow for a natural tapering of lobe distributions like Fig. 11. Once all the events have been identified, each is randomly assigned a direction and compatible source location from the results in Table 2. This is done to demonstrate the typical radiation properties of the lobes more clearly by removing extreme outliers that can occur in the EBBF processing. With event radiation locations calculated, a time delay is applied to each event that accounts for the time it takes for the acoustic event to travel from the lipline to the microphone. This is done to illustrate event timing at the source.

The animation has three components: propagating events, the current event fraction, and the cumulant event count. Radiating events are represented by colored arrows traveling from the jet lipline to the microphone array. These arrows travel at an assumed sound speed of 343 m/s. Before the arrows are drawn, upcoming events in the flow are represented by colored circles convecting at the jet exit velocity. Once the circle reaches its predetermined radiation location, it is drawn as an arrow and propagates to the microphone where the event was measured. Note that there are no fluid dynamic calculations or measurements used for the events within the plume boundaries.

In the upper left corner of the animation is a bar chart that depicts the current event fraction. These bars give a visual representation of the number of radiating events (arrows) in the current frame. This graph helps quantify the underlying relationships between the events, notably, the results from Sec. IV.C regarding the relationship between lobes. From the bar charts, the higher-ordered lobes are seen to exhibit more temporal overlap than the lower ones. As time progresses, lobes 1 and 2 frequently vanish entirely, with packets of events coming at longer intervals than the higher lobes. On the contrary, lobes 4 and 5 exhibit significant overlap in that these events are nearly always visible together. Lobe 3 falls between the two extremes.

Finally, the cumulant event count is plotted as an overlapping collection of histograms that represent the number of acoustic events that have been measured by the microphone array. These grow as the animation progresses and demonstrate the relative number of events present for each lobe within the presented time window. From the extracted histograms in Fig. 13a, it is seen that

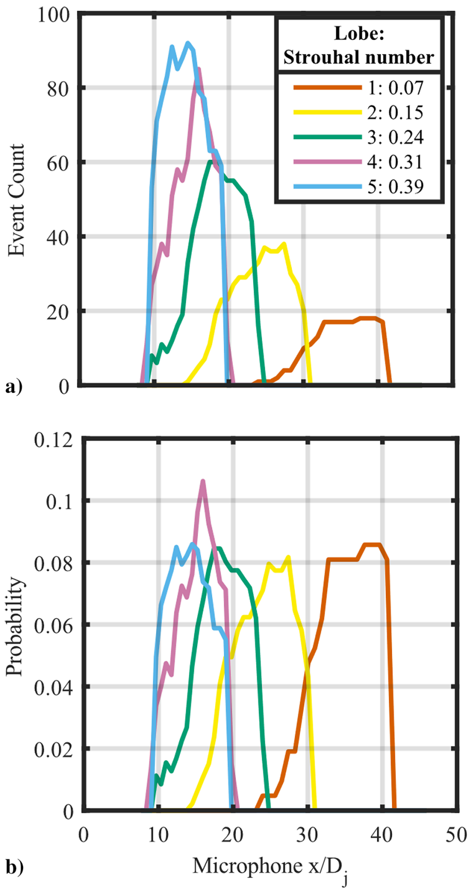

Fig 13 Long-term count (a) and probability (b) histograms corresponding to the number of events in each microphone along the imaging array.

most of the events fall primarily to the higher frequency lobes. While this might indicate that the higher-ordered lobes represent a larger portion of the energy in the signal, there is something to be said about the characteristic time scale of these events. Section IV.B shows that the characteristic event length is on the order of a few periods. Since higher frequencies correspond to a shorter period, events will have a more localized time signature, whereas lower frequency events will have longer time signatures. This means that for a given time window there will be more high-frequency events than low-frequency events. This difference is accounted for in Fig. 13b, where each plot is normalized into a probability density function (PDF). With this normalization, it becomes more apparent that the lobes are relatively uniformly distributed across their microphones, with the exception of lobe 4, which has a sharp peak at the overlap between lobes 3 and 5. Finally, the overlap of the lobes as presented here corroborates with what is seen in the measured spatiospectral maps in Fig. 1, as well as the decomposition in Fig. 11: the higher ordered lobes exhibit a strong spatial overlap while lobes 1 and 2 are spatially distinct.

E. Mechanisms for the Spatiospectral Lobes

After all this acoustical characterization, one question remains: What are the flow phenomena responsible for the spatiospectral lobe radiation? Due to the nature of the T-7A measurement, it was impossible to collect real-time flow data during the measurement. However, some theories can be presented here.

From Sec. III.A, lobe 1 was identified to behave differently from the higher-ordered lobes, which suggests its own production mechanism. While extensive work has not been done for this lobe, the downstream source location supports the possibility of scrubbing noise where the shear layer intersects the ground.

The source locations for the higher-ordered lobes are near the potential core tip and up to the supersonic core tip. This location suggests that the lobes may be related to Mach waves. One theory from previous work [8] supposes that the lobes could be generated by different families of Mach waves; however, the T-7A jet conditions at military power only support Kelvin–Helmholtz instability waves [40]. An alternative is some kind of interaction between the convecting turbulence and the shock cells, as postulated by Wall et al. [41]. One possibility could be between turbulent structure and shock cell Prandtl–Meyer expansion fans, as proposed by Swift et al. [42]. The quasi-periodic acceleration and deceleration would result in Mach wave radiation at different angles corresponding to the changing flow speed. Coherence analysis on this same aircraft has shown coherence between broadband shock-associated noise and the spatiospectral lobes [43,44], again suggesting an interaction between the lobes and the shock cells. This strong connection to the shock cells warrants future investigation.

The relation between the spatiospectral lobes and wavepackets is still an open question. While both feature temporospectrally discrete bursts of energy, events associated with the lobes oscillate between multiple frequencies, which is more closely related to a mode switching phenomenon. Future work should look at possible overlaps between these two temporal behaviors and how they can be related to the shock cells.

V. Conclusions

This paper has investigated the spatial, spectral, and temporal features of the spatiospectral lobes using a combination of analysis techniques. The EBBF algorithm, developed in a previous crackle study, has been implemented for the T-7A. The method has been enhanced by using a wavelet transform to identify frequency events in the time waveform related to the spatiospectral lobes. These events have been linearly traced back to the jet lipline to define apparent source locations of the spatiospectral lobes. The results have shown that individual lobes are radiation from overlapping sources with different directivities, which compares favorably to previous analysis. Lobe 1 is an exception and is theorized to be a different phenomenon than the other lobes.

A Markov-style analysis has been used to characterize the spatiotemporal structure of the lobes as seen in the wavelet power spectrum. Visually, events appear to switch between Strouhal numbers corresponding to notable peaks in the time-averaged spectrum. The switching behavior is reminiscent of mode switching in lab-scale jet screech, and the intermittency resembles the temporal intermittency of wavepackets. The Markov model has shown that events along multiple spectral peaks are distributed relatively independently of each other, with event durations on the order of a few periods. The spatiospectral lobes can be understood as rapid bursts of energy at important spectral peaks radiating at different directivities.

Using the Markov state sequence as a guide, individual spectra corresponding to events at specific Strouhal numbers have been created, allowing the spatiospectral lobes to be viewed independently. The process has been applied to the entire microphone array, decomposing the initial spatiospectral maps into individual lobes. The decomposed maps have shown that while the lobes are largely independent phenomena, there exists a spectral overlap between lobes 3, 4, and 5. Lobes 1 and 2 remain separate and distinct. The combined spatiospectrotemporal analysis has been presented as an animation that shows that the events for the spatiospectral lobes come in discrete, intermittent packets radiating at different angles.

A few theories for how the lobes are generated have been discussed. One theory suggests that the lobes are the result of different families of Mach waves, but this is unlikely due to the presence of spatiospectral lobes at engine conditions that don't support multiple families. A more likely explanation points toward interactions between turbulent structures and the shock cells. There is ample evidence that the shock cells are involved, from lobe source locations to coherence between the lobes and broadband shock-associated noise. Future work should focus on expanding these connections and determining the properties of the shock cells as they relate to the radiated sound field. Possible nonlinear interactions between the higher-ordered lobes are also worth studying. Finally, further investigation of the temporal intermittency seen here and how it relates to the temporal structure of wavepackets and mode switching is warranted.

Acknowledgments

This work is funded by the Office of Naval Research grant number N00014-21-1-2069, titled "Connecting Analyses of Installed Tactical Jet Engine Noise with Simulated and Laboratory-Scale Data," with project monitor Dr. Steven Martens (Code 351 Jet Noise Reduction). The authors would also like to thank the reviewers for their helpful feedback.

References

[1] Martens, S., and Spyropoulos, J. T., "Practical Jet Noise Reduction for Tactical Aircraft," *Proceedings of ASME Turbo Expo 2010*, June 2010. https://doi.org/10.1115/GT2010-23699

[2] Wall, A. T., Gee, K. L., Neilsen, T. B., McKinley, R. L., and James, M. M., "Military Jet Noise Source Imaging Using Multisource Statistically Optimized Near-Field Acoustical Holography," *Journal of the Acoustical Society of America*, Vol. 139, No. 4, 2016, pp. 1938–1950. https://doi.org/10.1121/1.4945719

[3] Wall, A. T., Gee, K. L., Neilsen, T. B., Harker, B. M., McInerny, S. A., McKinley, R. L., and James, M. M., "Investigation of Multi-Lobed Fighter Jet Noise Sources Using Acoustical Holography and Partial Field Decomposition Methods," *AIAA Aviation 21st AIAA/CEAS Aeroacoustics Conference*, AIAA Paper 2015-2379, 2015. https://doi.org/10.2514/6.2015-2379

[4] Neilsen, T. B., Gee, K. L., Wall, A. T., and James, M. M., "Similarity Spectra Analysis of High-Performance Jet Aircraft Noise," *Journal of the Acoustical Society of America*, Vol. 133, No. 4, 2013, pp. 2116–2125. https://doi.org/10.1121/1.4792360

[5] Harker, B. M., Neilsen, T. B., Gee, K. L., Wall, A. T., and James, M. M., "Spatiotemporal-Correlation Analysis of Jet Noise from a High-Performance Military Aircraft," *AIAA Journal*, Vol. 54, No. 5, 2016,

pp. 1554–1566.
https://doi.org/10.2514/1.J054442

[6] Tam, C. K. W., and Parrish, S. A., "Noise of High-Performance Aircraft at Afterburner," *Journal of Sound and Vibration*, Vol. 352, Sept. 2015, pp. 103–128.
https://doi.org/10.1016/j.jsv.2015.04.010

[7] Stout, T. A., Gee, K. L., Neilsen, T. B., Wall, A. T., and James, M. M., "Acoustic Intensity Near a High-Powered Military Jet Aircraft," *Journal of the Acoustical Society of America*, Vol. 138, No. 1, 2015, pp. EL1–EL7.
https://doi.org/10.1121/1.4921746

[8] Swift, S. H., Gee, K. L., Neilsen, T. B., Wall, A. T., Downing, J. M., and James, M. M., "Spatiotemporal Correlation Analysis of Jet Noise from a Round-Nozzle Supersonic Aircraft," *AIAA Aviation Forum, 2018 AIAA/CEAS Aeroacoustics Conference*, AIAA Paper 2018-3938, 2018.
https://doi.org/10.2514/6.2018-3938

[9] Leete, K. M., Wall, A. T., Gee, K. L., Neilsen, T. B., James, M. M., and Downing, J. M., "Acoustical Holography-Based Analysis of Spatiospectral Lobes in High-Performance Aircraft Jet Noise," *AIAA Journal*, Vol. 59, No. 10, 2021, pp. 4166–4178.
https://doi.org/10.2514/1.J059400

[10] Stout, T. A., Gee, K. L., Neilsen, T. B., Wall, A. T., and James, M. M., "Source Characterization of Full-Scale Jet Noise Using Acoustic Intensity," *Noise Control Engineering Journal*, Vol. 63, No. 6, 2015, pp. 522–536.
https://doi.org/10.3397/1/376346

[11] Olaveson, T., Ward, J., Johnson, J., Gee, K. L., and Wall, A. T., "Analysis of Spatiospectral Lobes in Installed F404 Engine Noise Radiation," *28th AIAA/CEAS Aeroacoustics Conference*, AIAA Paper 2022-3087, 2022.
https://doi.org/10.2514/6.2022-3087

[12] Padois, T., Gauthier, P. A., and Berry, A., "Inverse Problem with Beamforming Regularization Matrix Applied to Sound Source Localization in Closed Wind-Tunnel Using Microphone Array," *Journal of Sound and Vibration*, Vol. 333, No. 25, 2014, pp. 6858–6868.
https://doi.org/10.1016/j.jsv.2014.07.028

[13] Mathews, L. T., Gee, K. L., Leete, K. M., and Wall, A. T., "Acoustic Source Characterization of an Installed GE F404 Engine Using Near-Field Acoustical Holography," *28th AIAA/CEAS Aeroacoustics Conference*, AIAA Paper 2022-3028, 2022.
https://doi.org/10.2514/6.2022-3028

[14] Vaughn, A. B., Gee, K. L., Swift, S. H., Leete, K. M., Wall, A. T., Downing, J. M., and James, M. M., "Source Localization of Crackle-Related Events in Military Aircraft Jet Noise," *AIAA Journal*, Vol. 59, No. 6, 2021, pp. 2251–2261.
https://doi.org/10.2514/1.j059823

[15] Vaughn, A. B., Gee, K. L., Swift, S. H., Wall, A. T., Downing, J. M., and James, M. M., "Beamforming of Supersonic Jet Noise for Crackle-Related Events," *Proceedings of Meetings on Acoustics*, Vol. 35, No. 1, 2018, Paper 040003.
https://doi.org/10.1121/2.0000998

[16] Torrence, C., and Compo, G. P., "A Practical Guide to Wavelet Analysis," *Bulletin of the American Meteorological Society*, Vol. 79, No. 1, 1998, pp. 61–78.
https://doi.org/10.1175/1520-0477(1998)079<0061:APGTWA>2.0.CO;2

[17] Heeb, N., Mora, P., Kastner, J., Gutmark, E., Kailasanath, K., and Liu, J., "Mode Switching of Jet Noise Screech," *18th AIAA/CEAS Aeroacoustics Conference (33rd AIAA Aeroacoustics Conference)*, AIAA Paper 2012-2162, 2012.
https://doi.org/10.2514/6.2012-2162

[18] Kœnig, M., Cavalieri, A. V. G., Jordan, P., Delville, J., Gervais, Y., and Papamoschou, D., "Farfield Filtering and Source Imaging of Subsonic Jet Noise," *Journal of Sound and Vibration*, Vol. 332, No. 18, 2013, pp. 4067–4090.
https://doi.org/10.1016/j.jsv.2013.02.040

[19] Baars, W. J., and Tinney, C. E., "Shock-Structures in the Acoustic Field of a Mach 3 Jet with Crackle," *Journal of Sound and Vibration*, Vol. 333, No. 12, 2014, pp. 2539–2553.
https://doi.org/10.1016/j.jsv.2014.01.008

[20] Reichman, B. O., Gee, K. L., Neilsen, T. B., Swift, S. H., Wall, A. T., Downing, J. M., and James, M. M., "Acoustic Shock Formation in Noise Propagation During Military Aircraft Ground Run-Up Operations," *AIAA Journal*, Vol. 60, No. 7, 2022, pp. 4081–4088.
https://doi.org/10.2514/1.J060307

[21] Akamine, M., Okamoto, K., Teramoto, S., and Tsutsumi, S., "Conditional Sampling Analysis of High-Speed Schlieren Movies of Mach Wave Radiation in a Supersonic Jet," *Journal of the Acoustical Society of America*, Vol. 145, No. 1, 2019, pp. EL122–EL128.
https://doi.org/10.1121/1.5088493

[22] Von Hilgers, P., and Langville, A. N., "The Five Greatest Applications of Markov Chains," *Proceedings of the Markov Anniversary Meeting*, Boston Press, Boston, MA, 2006, pp. 155–168.

[23] Shannon, C. E., "A Mathematical Theory of Communication," *Bell System Technical Journal*, Vol. 27, No. 3, 1948, pp. 379–423.
https://doi.org/10.1002/j.1538-7305.1948.tb01338.x

[24] Scherr, A. L., "An Analysis of Time-Shared Computer Systems," Ph.D. Thesis, Massachusetts Inst. of Technology, Cambridge, MA, 1962.

[25] Henderson, J., "Finding Genes in DNA with a Hidden Markov Model," *Journal of Computational Biology*, Vol. 4, No. 2, 1997, pp. 127–141.
https://doi.org/10.1089/cmb.1997.4.127

[26] Bahl, L. R., Jelinek, F., and Mercer, R. L., "A Maximum Likelihood Approach to Continuous Speech Recognition," *IEEE Transactions on Pattern Analysis and Machine Intelligence*, Vol. PAMI-5, No. 2, 1983, pp. 179–190.
https://doi.org/10.1109/TPAMI.1983.4767370

[27] Brooks, S. P., "Markov Chain Monte Carlo Method and Its Application," *Journal of the Royal Statistical Society Series D: The Statistician*, Vol. 47, No. 1, 1998, pp. 69–100.
https://doi.org/10.1111/1467-9884.00117

[28] Leete, K. M., Vaughn, A. B., Bassett, M. S., Rasband, R. D., Novakovich, D. J., Gee, K. L., Campbell, S. C., Mobley, F. S., and Wall, A. T., "Jet Noise Measurements of an Installed Ge F404 Engine," *AIAA SciTech Forum*, AIAA Paper 2021-1638, 2021.
https://doi.org/10.2514/6.2021-1638

[29] Christian, M. A., Gee, K. L., Streeter, J. B., Wall, A. T., and Campbell, S. C., "Sound Power and Acoustic Efficiency of an Installed GE F404 Jet Engine," *JASA Express Letters*, Vol. 3, No. 7, 2023, Paper 073601.
https://doi.org/10.1121/10.0019866

[30] Bendat, J. S., and Piersol, A. G., *Random Data*, 4th ed., Wiley, Hoboken, NJ, 1987, Chap. 5.
https://doi.org/10.1002/9781118032428

[31] Jordan, P., and Colonius, T., "Wave Packets and Turbulent Jet Noise," *Annual Review of Fluid Mechanics*, Vol. 45, No. 1, 2013, pp. 173–195.
https://doi.org/10.1146/annurev-fluid-011212-140756

[32] Crow, S. C., and Champagne, F. H., "Oderly Structure in Jet Turbulence," *Journal of Fluid Mechanics*, Vol. 48, No. 3, 1971, pp. 547–591.
https://doi.org/10.1017/S0022112071001745

[33] Cavalieri, A. V. G., Daviller, G., Comte, P., Jordan, P., Tadmor, G., and Gervais, Y., "Using Large Eddy Simulation to Explore Sound-Source Mechanisms in Jets," *Journal of Sound and Vibration*, Vol. 330, No. 17, 2011, pp. 4098–4113.
https://doi.org/10.1016/j.jsv.2011.04.018

[34] Cavalieri, A. V. G., Jordan, P., Agarwal, A., and Gervais, Y., "Jittering Wave-Packet Models for Subsonic Jet Noise," *Journal of Sound and Vibration*, Vol. 330, Nos. 18–19, 2011, pp. 4474–4492.
https://doi.org/10.1016/j.jsv.2011.04.007

[35] Juvé, D., Sunyach, M., and Comte-Bellot, G., "Intermittency of the Noise Emission in Subsonic Cold Jets," *Journal of Sound and Vibration*, Vol. 71, No. 3, 1980, pp. 319–332.
https://doi.org/10.1016/0022-460X(80)90416-2

[36] Kearney-Fischer, M., Sinha, A., and Samimy, M., "Time-Domain Analysis of Excited Subsonic Jet Noise," *International Journal of Aeroacoustics*, Vol. 12, No. 4, 2013, pp. 387–421.
https://doi.org/10.1260/1475-472X.12.4.387

[37] Suzuki, T., and Colonius, T., "Instability Waves in a Subsonic Round Jet Detected Using a Near-Field Phased Microphone Array," *Journal of Fluid Mechanics*, Vol. 565, Oct. 2006, pp. 197–226.
https://doi.org/10.1017/S0022112006001613

[38] Mathews, L. T., and Gee, K. L., "Coherence-Based Acoustic Source Decomposition of Installed GE F404 Engine Noise," *AIAA Journal*, Vol. 62, No. 6, 2024, pp. 2186–2199.
https://doi.org/10.2514/1.J063543

[39] Olaveson, T. W., Gee, K. L., and Johnson, J. P., "Wavelet-Based Analysis of Spectral and Temporal Structures in F404 Engine Jet Noise," *AIAA Aviation Forum*, AIAA Paper 2023-3213, 2023.
https://doi.org/10.2514/6.2023-3213

[40] Gee, K. L., Olaveson, T. W., and Mathews, L. T., "Convective Mach Number Definition and Their Relationship to Full-Scale Supersonic Jet Noise Directivity," *AIAA Journal*, April 2024 (Submitted).

[41] Wall, A. T., Leete, K. M., Gee, K. L., Neilsen, T. B., James, M. M., and McKinley, R. L., "Preliminary Investigation of Multilobe Fighter Jet Noise Sources Using Acoustical Holography," *23rd AIAA/CEAS Aeroacoustics Conference*, AIAA Paper 2017-3520, 2017.
https://doi.org/10.2514/6.2017-3520

[42] Swift, S. H., and Gee, K. L., "Investigating Focusing of Mach Waves by Prandtl-Meyer Expansion fan as an Explanation for Some

Spatiospectral Lobe Phenomena," *Journal of the Acoustical Society of America*, Vol. 146, Oct. 2019, p. 3000.
https://doi.org/10.1121/1.5137389

[43] Epps, K. A., Olaveson, T., Gee, K. L., Wall, A. T., and Swift, S. H., "Near-Field Coherence Analysis of Noise from an Installed F404 Engine," *Journal of the Acoustical Society of America*, Vol. 152, Oct. 2022, Paper A257.
https://doi.org/10.1121/10.0016199

[44] Mathews, L. T., and Gee, K. L., "An Investigation of Shock Cell-Related Noise in an Installed, Full-Scale Tactical Jet Engine Using Acoustical Holography," *Journal of the Acoustical Society of America*, Vol. 154, Oct. 2023, Paper A325.
https://doi.org/10.1121/10.0023683

X. Zhang
Associate Editor